Analyst

PAPER

View Article Online
View Journal | View Issue

Cite this: *Analyst*, 2014, **139**, 1192

Acoustic focusing with engineered node locations for high-performance microfluidic particle separation†

Erika J. Fong,[ab] Amanda C. Johnston,[a] Timothy Notton,[cf] Seung-Yong Jung,[ce] Klint A. Rose,[a] Leor S. Weinberger[cde] and Maxim Shusteff*[a]

Received 7th January 2014
Accepted 10th January 2014

DOI: 10.1039/c4an00034j

www.rsc.org/analyst

Acoustofluidic devices for manipulating microparticles in fluids are appealing for biological sample processing due to their gentle and high-speed capability of sorting cell-scale objects. Such devices are generally limited to moving particles toward locations at integer fractions of the fluid channel width (1/2, 1/4, 1/6, *etc.*). In this work, we introduce a unique approach to acoustophoretic device design that overcomes this constraint, allowing us to design the particle focusing location anywhere within the microchannel. This is achieved by fabricating a second fluid channel in parallel with the sample channel, separated from it by a thin silicon wall. The fluids in both channels participate to create the ultrasound resonance, while only one channel processes the sample, thus de-coupling the fluidic and acoustic boundaries. The wall placement and the relative widths of the adjacent channels define the particle focusing location. We investigate the operating characteristics of a range of these devices to determine the configurations that enable effective particle focusing and separation. The results show that a sufficiently thin wall negligibly affects focusing efficiency and location compared to a single channel without a wall, validating the success of this design approach without compromising separation performance. Using these principles to design and fabricate an optimized device configuration, we demonstrate high-efficiency focusing of microspheres, as well as separation of cell-free viruses from mammalian cells. These "transparent wall" acoustic devices are capable of over 90% extraction efficiency with 10 μm microspheres at 450 μL min^{-1}, and of separating cells (98% purity), from viral particles (70% purity) at 100 μL min^{-1}.

1 Introduction

Compact devices that can perform rapid and complex analysis[1] on minute biological samples with minimal reagents are appealing for both field and benchtop applications. Sample preparation for such devices, however, remains a critical challenge.[2] For successful analysis of clinical and environmental samples, pre-processing is most often performed on the benchtop and entails mostly manual, time-consuming and labor-intensive techniques. The coming together of the scaling advantages inherent in microtechnology, with the need to speed up, automate, and integrate sample preparation and analysis, has led to intense effort in the development of microfluidic platforms for a variety of tasks, from particle filtration, cell sorting and separation, to surface-based assays and purification of biological analytes.[3–10] Concurrently with the tremendous proliferation of microfluidic technologies over the last 20 years, rapid progress has been made in adapting ultrasound for sample manipulation in sub-millimeter-scale fluidic networks.[11,12] Acoustofluidic approaches combine non-contact handling of fluid-suspended particles with the potential for high-throughput continuous processing.

The fundamental mechanism of using ultrasound to move microparticles across fluid streamlines was first demonstrated nearly 20 years ago by Feke and coworkers[13,14] and extended by Coakley *et al.*[15,16] Since then, ultrasound pressure fields have been used for a wealth of applications such as fluid pumping,[17] mixing,[18] immunoassays,[19] drug delivery,[20] and single-particle positioning,[21] to name only a few. By far the most widespread

[a]*Lawrence Livermore National Laboratory, 7000 East Ave., Livermore, CA, 94550 USA. E-mail: shusteff1@llnl.gov; Fax: +1-925-422-2783; Tel: +1-925-423-0733*

[b]*Department of Biomedical Engineering, Boston University, 44 Cummington St., Boston, MA, 02215 USA*

[c]*The Gladstone Institutes (Department of Virology and Immunology), 1650 Owens Street, San Francisco, CA 94158, USA*

[d]*Department of Biochemistry and Biophysics, University of California, San Francisco, CA 94158, USA*

[e]*QB3: California Institute for Quantitative Biology, University of California, San Francisco, CA 94158, USA*

[f]*Joint Graduate Group in Bioengineering, University of California, San Francisco, CA 94158, USA*

† Electronic supplementary information (ESI) available: Details and results of first generation (GEN1) device characterization, optimization of transducer attachment, and PCR protocol details. See DOI: 10.1039/c4an00034j

applications have been in separating and sorting biological and non-biological particles, using both bulk[22,23] and surface acoustic waves.[24–26]

Our motivation is fast, continuous-flow separation for automated sample processing, particularly for isolation of viruses. Enrichment and purification of viral particles typically requires multiple centrifugation steps which require significant hands-on time, and/or membrane-based filtering, which incurs substantial loss of virions. A high-throughput flow-through viral enrichment technology such as this acoustofluidic device can be advantageous for reducing hands-on time while enriching for the viral content of samples such as serum (clinical), wastewater (industrial), and sea-water (environmental) for subsequent analysis.

Acoustophoretic primary radiation forces (PRF) on fluid-suspended particles scale with the particle volume[27] (*i.e.* the third power of the particle diameter a), and are thus readily implemented for size-based separation. Moreover, among the various separation approaches available in microfluidic systems, acoustophoresis competes only with inertial focusing[28] for being the highest-throughput microfluidic size separation technique.[29]

In recent years, Lund type[11] acoustofluidic devices have gained prominence. Here the acoustic resonance is established orthogonal to the piezo transducer's actuation axis,[30] which makes it easy to observe focusing through the device's glass lid, and devices can be produced with high precision by means of standard microfabrication techniques.[31] Typically, the channel width and the acoustic actuation frequency are matched to create a half-wave resonance within the device, with its pressure node at the channel centerline. This geometry is somewhat limiting because it requires either a trifurcation at the outlet[11,32,33] or highly stable and precise flow control to cleanly steer the particles of interest into a separate outlet from the input fluid stream. Another class of devices makes use of precisely matched material layers to generate quarter-wave resonance within the fluid channel and drive particles toward a pressure node at or near a channel wall.[34–37] While this is advantageous for surface-binding assays, it is undesirable in situations where the aim is to efficiently extract or separate particles in a high-throughput fashion, since streamlines near the wall are slower-moving, and particles are more likely to adsorb to the surface.

We seek a device geometry in which the particle focusing node position is not constrained to the channel centerline or walls. We therefore present a novel acoustofluidic configuration that allows the position of the pressure node within the microchannel to be arbitrarily chosen. This is accomplished by subdividing the microchannel into two parts using a thin silicon wall which is virtually transparent to the ultrasound. This decouples the fluidic and acoustic boundaries, as both portions of the subdivided channel participate in the acoustic resonance, but particle manipulation takes place in only one of them. For a given device, the location of the wall and the dimensions of the channels on either side define the node position, allowing particle focusing off the centerline. For example, a single node can be generated at 40% of the separation channel width, something not usually possible (Fig. 1). Some of the design features incorporated here, such as acoustophoresis in subdivided channels,[38] and acoustically transparent membranes in large-scale acoustic devices[39,40] have been demonstrated by other investigators. Of note are several reports of asymmetric focusing within the microchannel,[41] where the node position in some cases can be dynamically controlled by multi-mode superposition[42] or phase[43,44] or frequency[45] shifting. None of these prior approaches, however, have achieved significant flow rates, thus being highly limited in sample throughput. The approach described here is unique in taking advantage of asymmetric focusing to achieve high-flow, high-efficiency particle separation. The capability of positioning the pressure node at a designed location relaxes the flow stability requirements, and improves overall robustness of operation.

In this work, we quantify the effect of wall thickness on focusing efficiency and device operation. We describe a simple *in situ* method to determine the optimal operating conditions for each device and quantify its performance characteristics, and demonstrate reliable fabrication of devices with consistent operating conditions. We characterize the device functionality using microspheres, and demonstrate its utility with biological samples by successfully separating cell-free Dengue viruses from human lymphocytes. Cells are extracted into a clean buffer stream separate from the viruses, accomplishing more efficient cell extraction and cleaner spatial separation, at five-fold greater volume throughput compared to previous work.[46]

2 Materials and methods

Device design

The fluid channels of our devices have a rectangular cross-section, anisotropically etched 200 μm deep into ⟨100⟩ silicon by deep reactive ion etching. The bypass channel is etched at the same time as the separation channel, with the single-crystal silicon separating wall remaining between them (Fig. 1). A borosilicate glass lid is anodically bonded to seal the channel, and the devices are diced apart, giving each chip overall dimensions of 70 × 9 × 1 mm. Ultrasound actuation is generated by a PZT piezoceramic (PSI-5A4E, Piezo Systems, Woburn, MA) glued to the silicon side with cyanoacrylate. The overall fluidic geometry follows the H-filter paradigm,[47,48] with two inlets and two outlets for the main separation channel. The chips operate at the second harmonic (full-wave resonance), since stronger primary radiation forces (F_{rad}) are generated by operating at a higher frequency.[27] During device operation, sample and buffer solutions flow through the separation channel, while the bypass channel is filled with water.

Here we report on experimental results from two device generations. First-generation (GEN1) devices were designed to determine the effect of wall thickness and placement on acoustophoretic performance, and to choose design parameters that enable efficient high-throughput separation. Since the wall location cannot be dynamically adjusted within a single device,

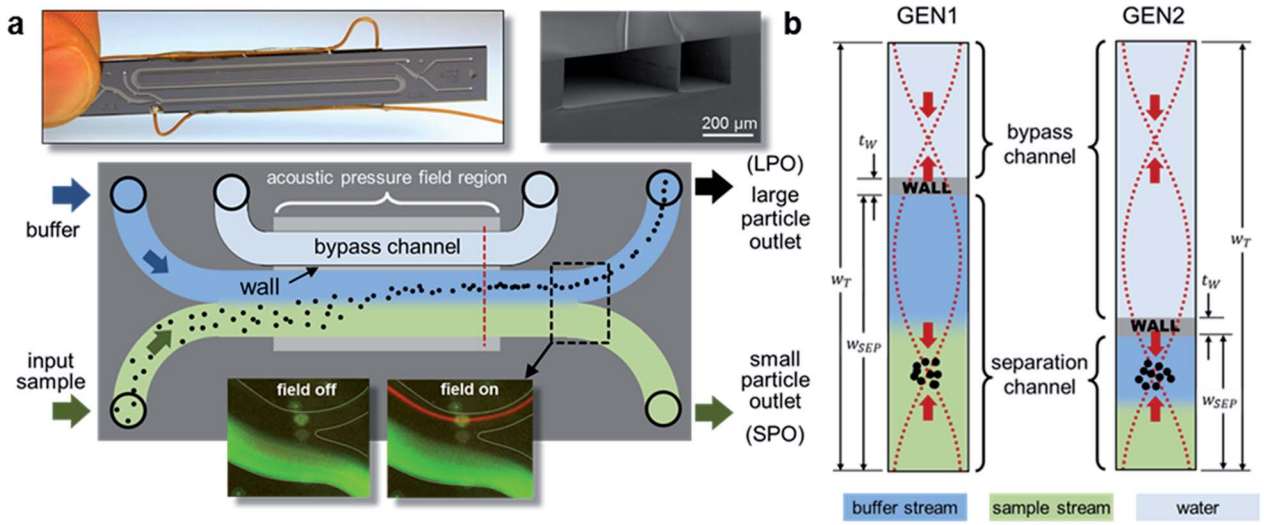

Fig. 1 Schematic sketches of "through the wall" acoustophoretic device architecture. (a) Top view, showing the overall H-filter configuration, with relative channel locations. Two fluid streams flow side-by-side in a separation channel, with a parallel bypass channel separated by a thin silicon wall. The inset at the top left is a photo of a GEN2 chip with three passes of the channel through the ultrasound field, and at the top right, an SEM image of the channel cross-section, showing the subdividing wall. The insets at the bottom are fluorescent micrographs of a mixture of 10 μm red-fluorescent and 200 nm green-fluorescent beads flowing out of the device outlet. (b) Schematic drawings of the channel cross-section at the location marked by the red dashed line in (a), showing the relative locations of the sample, buffer and bypass streams, and acoustic pressure node locations for GEN1 and GEN2 devices. The red dotted lines represent the full-wave ($n = 2$) pressure field in the channels and the red arrows indicate the sense of the acoustic primary radiation forces (PRF) that drive particles toward nodal planes.

wall thicknesses t_W of 16, 24, 32, 40, and 80 μm were fabricated, and separation channel widths w_{SEP} of 750 and 650 μm tested for each wall width. The combined channel widths w_T spanned 1 mm for all the devices, and focusing performance was compared to a 1 mm wide channel with no wall. The separation channel length for all GEN1 devices was 40 mm. For characterization of acoustic focusing, microsphere suspensions were injected into the inlet farthest from the bypass channel ("input sample" in Fig. 1a) such that particles starting out near the dividing wall would not be driven against it (see "GEN1" in Fig. 1b).

A second generation (GEN2) of devices was optimized in several different ways to achieve high-throughput particle size separation. First, by using the smaller channel as the separation channel, the F_{rad} force vectors point away from channel walls at all locations where particles pass (Fig. 1b). Second, these devices incorporate the thinnest walls that can be reliably fabricated without defects – 16 μm thick. Finally, the channels of GEN2 devices make three switchback passes down the microfluidic chip, with a total channel length of 117 mm, increasing sample residence time in the acoustic pressure field. In GEN2 devices, the total fluid channel width w_T is 900 μm, with separation channel widths w_{SEP} of 300 μm and 280 μm. As in the GEN1 devices, the sample to be processed is introduced on the side farthest from the bypass channel, with the largest particles migrating into the clean buffer stream for extraction out of the large-particle outlet (LPO), while smaller particles do not experience sufficient acoustic force, remaining in the input stream (SPO). Lengths of small-diameter FEP tubing (IDEX, 0.006″ ID) are attached at the outlets to provide modest back-pressure, thereby controlling the flow rate ratio between the separation channel outlets and increasing robustness against flow disturbances.

Experimental setup

All experiments were carried out on an inverted fluorescence microscope (Axiovert S100, Zeiss, Jena, Germany) with the acoustofluidic chip clamped to a custom-machined stage interface board, and tubing attached using custom gasketed fluidic fittings.[49] A function generator (33220A, Agilent, Santa Clara, CA) provided the sinusoidal excitation signals, amplified by an RF amplifier (410LA, ENI) to drive the piezo actuator. A cooled CCD camera (CoolSnap HQ2, Photometrics, Tucson, AZ) captured fluorescence images. Samples were pumped through the device by conventional syringe pumps (PHD 2000, Harvard, Holliston, MA) or by high-precision metering syringe pumps (microFlow, Micronics, Redmond, WA) connected to the device *via* multi-port valves (VICI Valco Instruments, Houston, TX) to enable selecting among sample, buffer, and cleaning solutions.

Several recent reports have emphasized the importance of temperature control for stable acoustophoretic device operation.[29,50] Operating un-cooled, our device temperature can rise to 70 °C or higher, so we use a small fan attached approximately 2 cm above the device to provide air cooling. This open-loop cooling approach is less complex than active feedback thermoelectric temperature control, and provides sufficient stability, limiting temperature variations to less than 2 °C for a given frequency and driving voltage, based on attached thermocouple measurements.

In situ calibration and performance characterization

To evaluate device performance, an *in situ* calibration method was developed to find the optimal focusing frequency f_0 for each chip and quantify the quality of focusing. This method is a

valuable supplement to analytical predictions based on geometric calculations, accounting for any temperature effects and variations in fabrication or piezo attachment. For this procedure a 0.01% (w/v) suspension of 5.78 μm fluorescent polystyrene beads (Bangs Laboratories, Fishers, IN) is pumped through the device at an average linear speed of 6 mm s^{-1} through the separation channel, while stepping through a range of driving frequencies (approx. 1.3–1.8 MHz) at 20 V_{pp}, and capturing fluorescent images at each frequency step for a straight channel region near the device outlet. Equilibration time after each frequency step is 10 seconds. The procedure is fully automated in LabView (National Instruments, Austin, TX), and captures a data-set in approximately 10 minutes. Images are post-processed in MATLAB (The MathWorks, Natick, MA) by averaging intensity values along the channel length dimension, generating a cross-sectional bead concentration profile at each frequency. When these profiles are combined into a heat-map plot as a function of frequency (Fig. 2), the optimal focusing frequency f_0 is usually apparent to the eye. In cases where f_0 is less obvious due to poor focusing, MATLAB chooses f_0 as the maximum amplitude point.

For a quantitative measure of particle focusing in GEN1 devices, focusing efficiency is calculated by integrating the intensity profile within ±25 μm of the peak location, normalized by the total intensity within the channel (not all GEN1 devices exhibited high quality focusing with Gaussian single-peak, intensity profiles). Higher values reflect better performance. For GEN2 devices, a Gaussian is fitted to the intensity profile at the peak frequency, and the full width at half maximum (FWHM) is used as a measure of focusing efficiency, with lower values representing better performance. Having attained greater reliability in device fabrication and piezo attachment with GEN2, we evaluated their repeatability by making multiple measurements of peak location and FWHM at f_0 at linear flow velocities of 20 and 60 mm s^{-1}, corresponding to 33 and 100 μL min^{-1}. For each of the GEN2 device configurations, two chips were tested for a minimum of $n = 6$ experiments.

High throughput focusing

Seeking to explore the performance limits of this device at high flow rates, a suspension with a mixture of particle sizes was prepared (diameters 2.04, 3.10, 5.78, 9.96, 12.01 and 15.02 μm, with approx. 10^8 beads mL^{-1} each) and processed through a 3-pass GEN2 chip with $w_{SEP} = 300$ μm, at 16 V_{pp} driving voltage. Sample inlet flow rates between 100 and 810 μL min^{-1} were tested ($n = 3$), corresponding to total flows in the separation channel between 200 μL min^{-1} and 1.6 mL min^{-1}, and equivalent to average flow speeds of 60 to 450 mm s^{-1}. Processed samples were collected from both outlets of the separation channel and their bead content quantified by flow cytometry (Microcyte, Aber Instruments, Wales). The extraction purity for each flow rate and particle size was calculated as the percentage of particles collected from the LPO relative to the total particle count collected from both outlets.

Cell-virus separations

As a demonstration of the benefit of these devices for size-separating biological particles, experiments were carried out with mixtures of cultured human Raji lymphocytes (5–8 μm diameter[51]) and Dengue virus particles (50 nm diameter[52]). Raji cells (ATCC, Manassas, VA) were cultured in RPMI 1640 growth media supplemented with 10% fetal bovine serum at 37 °C and 5% CO_2. For experiments, cells were re-suspended in 1× PBS. Cells were kept at room temperature during experiments. Dengue virus, serotype 2 (DENV2) was grown in Vero cells, purified, concentrated to an estimated 10^8 PFU per mL, and kept as frozen stock at −80 °C until needed for experiments.

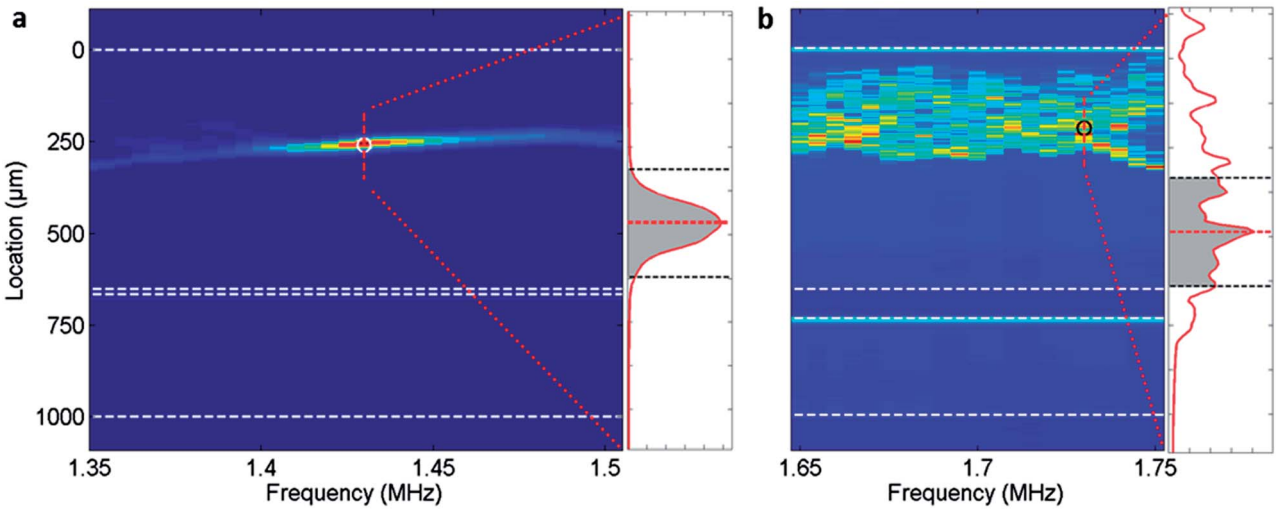

Fig. 2 Representative heat-map plots from the results of *in situ* frequency sweeps for GEN1 devices with $w_{SEP} = 650$ μm and (a) 16 μm and (b) 80 μm walls. Channel walls are outlined with white dashed lines and peak frequencies and locations are indicated by circles, with the intensity profile for the segment indicated by the red dashed line at each peak frequency shown in the insets. The shaded area within ±25 μm of the peak location is used for quantifying focusing efficiency. The focusing efficiencies are 0.901 and 0.294 respectively.

Control experiments were first carried out with pure virus and pure cell samples to determine baseline results when the two particle types do not interact with each other. Then cell samples (approx. 10^5 mL^{-1}) were spiked with viruses (approx. 10^5 PFU per mL), and processed through the device. Whole viruses were diluted 1 : 1000 from frozen stock into either 1× PBS (virus only experiments) or Raji cell suspensions (spiked experiments). Three trials were carried out for each of the pure and spiked samples with the acoustic field both on and off. A 3-pass GEN2 device with $w_{SEP} = 300$ μm was used for these experiments, at 100 μL min^{-1} sample flow rate, and 16 V_{pp} driving voltage when the acoustic field was active. Prior to processing each set of samples, the fluidic system was incubated with fresh cell media for a minimum of 20 minutes, to coat interior chip and tubing surfaces, thereby minimizing nonspecific cell and virus adsorption. Cell quantitation before and after sample processing was accomplished by Coulter counting (Z2, Beckman Coulter). Relative viral load was measured by quantitative reverse-transcription polymerase chain reaction (qRT-PCR), comparing threshold cycle (C_T) values of collected samples to input C_T values in order to determine the percentage exiting each outlet. The PCR protocol and the primer and probe sequence details are given in Section S2 (ESI†).

3 Results

Focusing and separation characteristics

Section S1 and Fig. S1 (ESI†) provide the complete results and detailed discussion of focusing measurements performed with GEN1 devices. In brief, most of the measured data supported the expected trends: devices with greater wall thickness t_W have higher resonant frequencies f_0, and reduced focusing efficiency. In addition, the focusing location within devices with thinner walls is more predictable and in better agreement with calculations. These results informed the design choice within GEN2 devices to use the thinnest reliably fabricated walls (16 μm). Minimizing the wall thickness t_W ensures that the effects of the wall on focusing position, operating frequency, and separation efficiency can be neglected.

In second generation devices, in addition to characterizing the overall device performance and reliability across multiple chips, we evaluated the benefit of three passes of the fluid channel down the chip (117 mm total length) by comparing the performance to identical 40 mm long devices (1-pass $w_{SEP} = 300$ μm), shown in Fig. 3. As expected, single-pass devices perform less well than three pass devices, requiring higher voltages to approach the node position, and never achieving the same tightness of focusing. Notably, there is good agreement between experiments in which beads have approximately the same on-chip residence time, in single-pass devices at 20 mm s^{-1} (red circles, dotted lines) and three-pass devices at 60 mm s^{-1} (blue squares, dashed lines). Therefore, the beads' lateral migration speed across streamlines is consistent between the different devices, and these data serve to validate the robustness of the overall design approach. Similarly significant is the comparison between identical GEN2 devices with their wall locations differing by 20 μm, shown in Fig. S3.† There is no meaningful difference between the

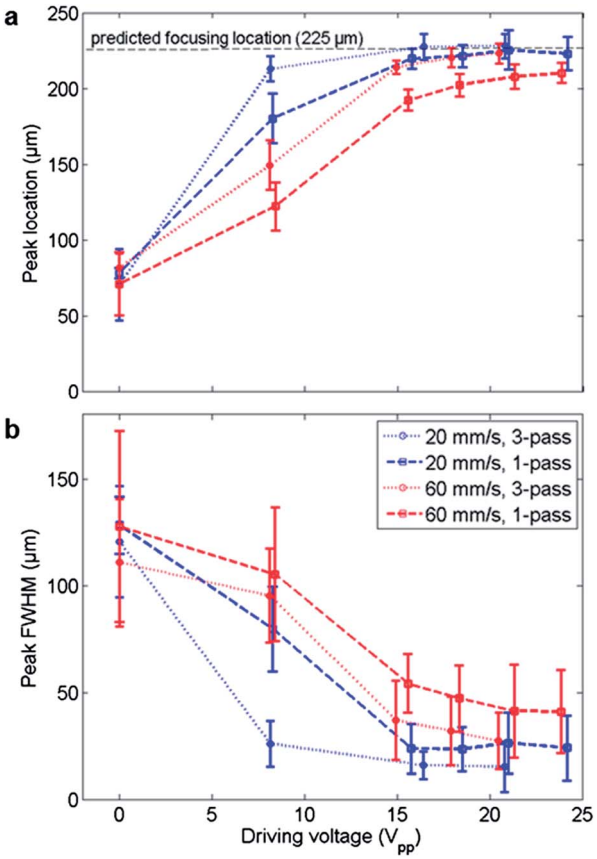

Fig. 3 *In situ* characterization data comparing 1-pass and 3-pass GEN2 devices, showing (a) peak location and (b) focusing width. Average linear flow velocity for points shown in red was 60 mm s^{-1} and blue 20 mm s^{-1}. Data for 1-pass devices represents at least $n = 6$ measurements, while for the 3-pass devices, $n = 12$ or greater.

focusing locations and efficiencies in these devices, confirming that the acoustic resonance can be designed with no effect from the wall.

The data in Fig. 3 also indicate the similarities across all three GEN2 designs. At higher operating voltages, particles migrate closer to the predicted focusing location approximately 225 μm away from the wall ($w_{eff}/4$), and the FWHM of the focused particle stream tightens. Peak frequencies f_0 increase slightly with higher driving voltages (data not shown), as expected due to an increase in operating temperature and thus an increase in the speed of sound. The maximum variation in peak frequency with driving voltage is a difference of 0.03 MHz between 8 V_{pp} and 23 V_{pp} (approx. 25–42 °C). We also see no meaningful difference in focusing performance between devices with $w_{SEP} = 280$ μm and 300 μm (Fig. S3 in the ESI†). Finally, the data with the field off (0 V_{pp}) do not show a difference between the single-pass and three-pass chips, indicating that the serpentine design does not introduce significant mixing (*e.g.* by Dean vortices) to degrade separation performance at flow speeds up to 60 mm s^{-1}.

Fig. 4 shows the extraction results for separating microspheres of different sizes at high flow speeds. Significantly, 10 μm beads are extracted at 90% efficiency even at 250 mm s^{-1},

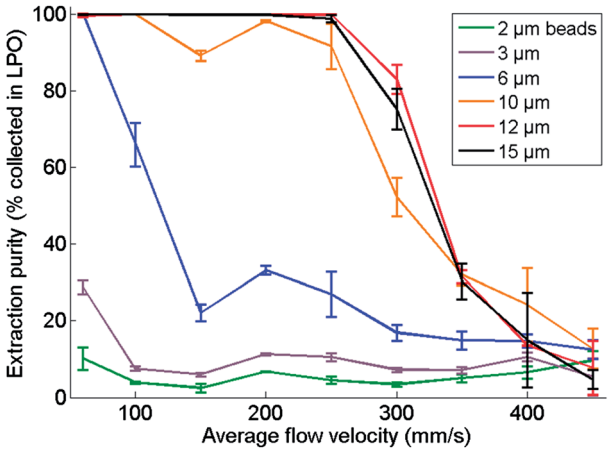

Fig. 4 Extraction of polymer microspheres of different sizes in the LPO (clean buffer stream) at high flow rates, using a 3-pass, w_{SEP} = 300 μm GEN2 device, at a driving voltage of 16 V_{pp}, $n = 3$ or greater.

which corresponds to a sample input flow of 450 μL min^{-1}. With buffer flowing at the same rate, the total flow is 900 μL min^{-1}. To the authors' knowledge this is the greatest linear flow velocity and one of the highest volumetric flow rates among any acoustophoretic devices that have been reported to-date. Additional separation data from experiments with GEN2 devices at different operating voltages is shown in Fig. S4 (ESI†), along with a Video (S2) showing the real-time separation of 10 μm and 200 nm fluorescent microspheres.

Cell-virus separations

Fig. 5 presents the separation results of processing Raji cells and Dengue viruses through the chip. The black-outlined segment of each bar represents the outlet from which those particles are intended to exit. With the acoustic field on, cells

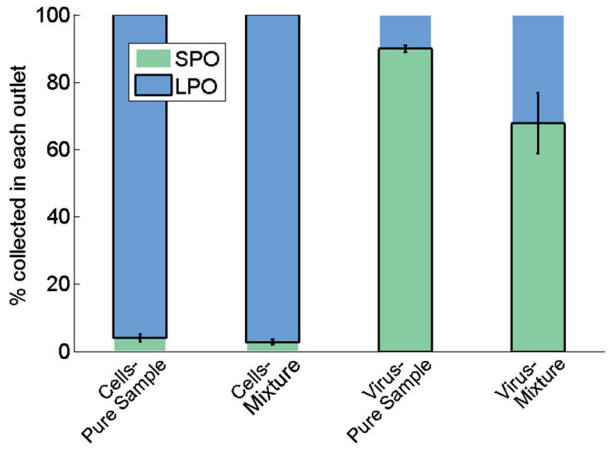

Fig. 5 Fraction of collected bio-particles extracted in the small (SPO) and large (LPO) particle outlet when operated at 16 V_{pp}. Thick black borders indicate the intended outlet for each particle type. Error bars are one standard deviation, $n = 3$. When the acoustic field is off, greater than 98% of all particles exit from the SPO in both purified or mixed conditions.

are successfully extracted into the clean buffer stream, at over 97% purity for cell-only samples as well as for cells spiked with virus (Fig. 5, "Cells-Pure Sample" and "Cells-Mixture"). Viruses, however are more likely to move into the clean buffer stream when cells are present in the solution. Without cells, only 10% of viruses are collected at the LPO, whereas with cells present, this figure rises to 32% (Fig. 5, "Virus-Pure Sample" and "Virus-Mixture"). With the acoustic field turned off, the cells and virus are collected at over 97% purity in the SPO, with less than 2% of either cells or viruses exiting from the LPO, indicating very low diffusion across streamlines.

4 Discussion

The results of this study provide validation for the "transparent wall" approach to acoustofluidic device design. As intended, the subdivision of the resonant fluid volume allows the effective decoupling of the acoustic and fluidic boundaries of the device. Asymmetric placement of a single pressure node is possible, by choosing a resonance condition for the overall combined channel, while disregarding the dimensions of the two sub-channels, and placing the subdividing wall in the location optimal for the separation. Although beyond the scope of the present work, the use of fluids other than water in the bypass channel lends additional flexibility to this design methodology. The results of the study with GEN1 chips yield useful practical parameters for using this approach to design a high-efficiency particle separator. The GEN1 results also highlight the importance of reliable transducer attachment.

The overall trends among the GEN1 devices suggest that thinner walls lead to improved focusing efficiency and closer correspondence between predicted (calculated) and measured focusing location and frequency. Moreover, though thicker-wall chips presented significantly different results for different separation channel widths w_{SEP}, chips with thinner walls showed greater consistency (smaller error bars) for all focusing metrics. This suggests that even with suboptimal coupling of the piezo transducer, thin-walled chips (20 μm or less) behave very nearly like devices without walls. We hypothesize that the vibrational modes of the walls themselves (acting as a plate resonator at frequencies different from the overall channel resonance) interfere with particle focusing when walls are thicker and have greater mass. More massive walls propagate more acoustic energy at non-focusing frequencies, interfering with efficient transmission of energy at the focusing frequency. We have seen partial evidence for this supposition in a limited numerical study using finite-element methods (data not shown), which will require further investigation within the context these designs. The present empirical study nevertheless provides the acoustofluidic device engineer with reliable design parameters for laying out fluid channel networks with predictably positioned off-center nodal locations.

Equipped with these design parameters, we have successfully optimized a through-the-wall type device for high-flow bioparticle separation, as demonstrated with the second device generation. The reliability and robustness of the design is evident from the consistent focusing performance across 6

Table 1 Volume throughput and flow speed of the present device design in comparison to previously-reported high-throughput acoustophoretic separators

Reference	Sample inlet flow rate (μL min^{-1})	Total flow rate (μL min^{-1})	Channel cross-sectional dimensions W × H (μm)	Maximum separation channel flow speed (mm s^{-1})
This work	450	900	300 × 200	250
Adams *et al.*, 2012[29]	16 667	50 000	17 000 × 830	59
Augustsson *et al.*, 2012[54]	70	560	375 × 150	166
Yang and Soh, 2012[53]	67	267	350 × 56	228
Petersson *et al.*, 2007[55]	40	400	370 × 125	144
Hawkes *et al.*, 2004[16]	10 200	10 200	10 000 × 250	68
Petersson *et al.*, 2004[23]	200	200	350 × 125	76

devices seen in Fig. 3 and S3 (ESI†). Furthermore, as intended, this design approach achieves excellent separation performance at very high flow rates. Table 1 summarizes flow data form some of the highest-throughput devices reported to-date. The data is selected for conditions at which the devices achieved 90% or better extraction of 10 μm (or similar) particles. Flow velocity is calculated from channel dimensions and the total volume passing through the channel where the acoustic pressure field is active, taking into account sample and any co-flowing buffer. The present design not only attains the highest flow speed in the separation channel, but has one of the highest volume throughputs as well. While volume throughput is certainly a critical metric, the flow speed is perhaps a more direct measure of how efficiently the acoustic field moves particles within the channel. Significantly, the devices that come closest to matching the present design in linear velocity lag far behind in sample flow rate (6–10× lower) due to much smaller channel dimensions[53] or high dilution factors.[54,55] The approach in the present work is therefore a unique combination of high separation efficiency with high throughput.

These devices also show high separation efficiency when manipulating biological particles. Acoustic actuation efficiently extracts Raji cells from the input stream into a separate outlet (Fig. S5†). This is in line with a multitude of recent reports of efficient acoustophoretic manipulation of many different cell types.[33,53,54] The goal for viral particles is that they will not be moved by the acoustic field, remaining in the original fluid stream and exiting in the SPO. Overall, this is how the virions behave, but the full picture is more nuanced. When the acoustic field is turned on, many more viral particles exit from the LPO than when the field is off, even for pure viral samples (less than 2% with no field, and 10% at 16 V_{pp}). We conjecture that this is due to acoustic streaming, which dominates the transport of submicron particles and generally requires high actuation power to induce appreciable particle movement.[56] We see some evidence to support this conjecture in Fig. S2,† where approximately 10% of the smallest particles are extracted at the highest actuation power. However, a more thorough investigation of the contributions from acoustic streaming in these devices (*e.g.* by micro-particle image velocimetry) is beyond the scope of the present work.

Moving beyond purified viral samples, adding cells into the sample mixture increases the fraction of viral genetic material detected in the LPO to approximately 30%, thereby limiting separation efficiency (Fig. 5). This is to be somewhat expected as cells migrating across streamlines due to the acoustic radiation force can drag the much smaller viral particles with them, and induce fluid transfer from the sample stream to the buffer stream, despite low Reynolds numbers. In addition, because Raji lymphocytes are a target cell type for DENV2, some viruses are likely attaching to cell membrane antigen receptor sites and migrating into the LPO along with the cells. In our experiments, significant cell infection (viral entry into cells) is not expected to take place, as viruses were spiked into the cell suspension shortly before separation, giving the viruses and cells no more than 20 minutes together. However, membrane attachment even without viral entry will result in increased viral genetic material being detected in the LPO. These results suggest an intriguing direction for further investigation with these devices, in which careful control over mixing, pre-incubation, and separation time can yield new insight into the kinetics of viral attachment and infection.

5 Conclusions

In summary, we have successfully designed and implemented an acoustic separation microdevice with the unique feature of custom-designed asymmetric node positioning within the separation channel. This has the benefits of relaxed flow and temperature control requirements, and reduced acoustic power demands, while enabling extremely high-throughput particle size sorting, and high-purity separation of biological particles. We have confirmed the validity of this design approach by fabricating a variety of devices of this type and exploring their focusing performance for a range of geometrical parameters. Guided by these performance results, an optimized design successfully demonstrated its high-speed separation capabilities, and its utility for enriching viral particles from mixtures of cells and viruses. We anticipate useful application of these devices in many contexts in which enrichment or purification of viral particles from mixed and particle-contaminated samples is required.

Acknowledgements

The authors are grateful to José Peña and Pejman Naraghi-Arani for the use of viral samples as well as PCR probe and primer sequences, and Cindy Thomas for cell samples. We thank Sally Hall for her PCR expertise, Dietrich Dehlinger for designing the automated image capture procedure, and Raymond P. Mariella,

Jr and Elizabeth Wheeler for invaluable discussions and feedback. We likewise thank Julie Hamilton and Elaine Behymer for their fabrication skills and cleanroom expertise. This work was performed under the auspices of the U.S. Department of Energy by Lawrence Livermore National Laboratory under Contract DE-AC52-07NA27344. EJF acknowledges support from the Lawrence Scholar Program at LLNL. MS and LSW acknowledge support from the UC Office of the President Lab Fees Research Program [Award #A119781 (Weinberger)]. LLNL-JRNL-640796.

References

1 F. Olasagasti and J. C. Ruiz de Gordoa, *Transl. Res.*, 2012, **160**, 332–345.
2 R. Mariella, Jr, *Biomed. Microdevices*, 2008, **10**, 777–784.
3 N. Pamme, *Lab Chip*, 2007, **7**, 1644.
4 J. Kim, M. Johnson, P. Hill and B. K. Gale, *Integr. Biol.*, 2009, **1**, 574.
5 C. D. Chin, T. Laksanasopin, Y. K. Cheung, D. Steinmiller, V. Linder, H. Parsa, J. Wang, H. Moore, R. Rouse, G. Umviligihozo, E. Karita, L. Mwambarangwe, S. L. Braunstein, J. van de Wijgert, R. Sahabo, J. E. Justman, W. El-Sadr and S. K. Sia, *Nat. Med.*, 2011, **17**, 1015–1019.
6 A. A. S. Bhagat, H. Bow, H. W. Hou, S. J. Tan, J. Han and C. T. Lim, *Med. Biol. Eng. Comput.*, 2010, **48**, 999–1014.
7 J. W. Hong, V. Studer, G. Hang, W. F. Anderson and S. R. Quake, *Nat. Biotechnol.*, 2004, **22**, 435–439.
8 M. Toner and D. Irimia, *Annu. Rev. Biomed. Eng.*, 2005, **7**, 77–103.
9 A. Lenshof and T. Laurell, *Chem. Soc. Rev.*, 2010, **39**, 1203–1217.
10 Y. Dong, A. M. Skelley, K. D. Merdek, K. M. Sprott, C. Jiang, W. E. Pierceall, J. Lin, M. Stocum, W. P. Carney and D. A. Smirnov, *J. Mol. Diagn.*, 2013, **15**, 149–157.
11 T. Laurell, F. Petersson and A. Nilsson, *Chem. Soc. Rev.*, 2007, **36**, 492.
12 A. Lenshof, C. Magnusson and T. Laurell, *Lab Chip*, 2012, **12**, 1210–1223.
13 Z. I. Mandralis and D. L. Feke, *AIChE J.*, 1993, **39**, 197–206.
14 D. A. Johnson and D. L. Feke, *Sep. Technol.*, 1995, **5**, 251–258.
15 J. J. Hawkes and W. T. Coakley, *Enzyme Microb. Technol.*, 1996, **19**, 57–62.
16 J. J. Hawkes, R. W. Barber, D. R. Emerson and W. T. Coakley, *Lab Chip*, 2004, **4**, 446.
17 A. R. Tovar, M. V. Patel and A. P. Lee, *Microfluid. Nanofluid.*, 2011, **10**, 1269–1278.
18 T.-D. Luong, V.-N. Phan and N.-T. Nguyen, *Microfluid. Nanofluid.*, 2011, **10**, 619–625.
19 M. Wiklund, S. Radel and J. J. Hawkes, *Lab Chip*, 2012, **13**, 25–39.
20 D. Carugo, D. N. Ankrett, P. Glynne-Jones, L. Capretto, R. J. Boltryk, X. Zhang, P. A. Townsend and M. Hill, *Biomicrofluidics*, 2011, **5**, 044108.
21 S. Oberti, D. Möller, A. Neild, J. Dual, F. Beyeler, B. J. Nelson and S. Gutmann, *Ultrasonics*, 2010, **50**, 247–257.
22 M. V. Patel, A. R. Tovar and A. P. Lee, *Lab Chip*, 2011, **12**, 139–145.
23 F. Petersson, A. Nilsson, C. Holm, H. Jönsson and T. Laurell, *Analyst*, 2004, **129**, 938.
24 J. Nam, H. Lim, D. Kim and S. Shin, *Lab Chip*, 2011, **11**, 3361–3364.
25 M. Gedge and M. Hill, *Lab Chip*, 2012, **12**, 2998–3007.
26 J. Shi, H. Huang, Z. Stratton, Y. Huang and T. J. Huang, *Lab Chip*, 2009, **9**, 3354–3359.
27 H. Bruus, *Lab Chip*, 2012, **12**, 1578–1586.
28 G. Guan, L. Wu, A. A. Bhagat, Z. Li, P. C. Chen, S. Chao, C. J. Ong and J. Han, *Sci. Rep.*, 2013, **3**, 1475.
29 J. D. Adams, C. L. Ebbesen, R. Barnkob, A. H. J. Yang, H. T. Soh and H. Bruus, *J. Micromech. Microeng.*, 2012, **22**, 075017.
30 A. Nilsson, F. Petersson, H. Jönsson and T. Laurell, *Lab Chip*, 2004, **4**, 131.
31 A. Lenshof, M. Evander, T. Laurell and J. Nilsson, *Lab Chip*, 2012, **12**, 684–695.
32 P. Augustsson, J. Persson, S. Ekström, M. Ohlin and T. Laurell, *Lab Chip*, 2009, **9**, 810.
33 F. Petersson, A. Nilsson, C. Holm, H. Jönsson and T. Laurell, *Lab Chip*, 2005, **5**, 20.
34 J. J. Hawkes, M. J. Long, W. T. Coakley and M. B. McDonnell, *Biosens. Bioelectron.*, 2004, **19**, 1021–1028.
35 S. P. Martin, R. J. Townsend, L. A. Kuznetsova, K. A. J. Borthwick, M. Hill, M. B. McDonnell and W. T. Coakley, *Biosens. Bioelectron.*, 2005, **21**, 758–767.
36 P. Glynne-Jones, R. J. Boltryk, M. Hill, N. R. Harris and P. Baclet, *J. Acoust. Soc. Am.*, 2009, **126**, EL75.
37 R. J. Townsend, M. Hill, N. R. Harris and M. B. McDonnell, *Ultrasonics*, 2008, **48**, 515–520.
38 O. Manneberg, S. Melker Hagsäter, J. Svennebring, H. M. Hertz, J. P. Kutter, H. Bruus and M. Wiklund, *Ultrasonics*, 2009, **49**, 112–119.
39 O. Doblhoff-Dier, T. Gaida, H. Katinger, W. Burger, M. Groschl and E. Benes, *Biotechnol. Prog.*, 1994, **10**, 428–432.
40 J. J. Hawkes, M. S. Limaye and W. T. Coakley, *J. Appl. Microbiol.*, 1997, **82**, 39–47.
41 S. Kapishnikov, V. Kantsler and V. Steinberg, *J. Stat. Mech.: Theory Exp.*, 2006, **2006**, P01012.
42 P. Glynne-Jones, R. J. Boltryk, N. R. Harris, A. W. J. Cranny and M. Hill, *Ultrasonics*, 2010, **50**, 68–75.
43 L. Meng, F. Cai, Z. Zhang, L. Niu, Q. Jin, F. Yan, J. Wu, Z. Wang and H. Zheng, *Biomicrofluidics*, 2011, **5**, 044104.
44 N. D. Orloff, J. R. Dennis, M. Cecchini, E. Schonbrun, E. Rocas, Y. Wang, D. Novotny, R. W. Simmonds, J. Moreland, I. Takeuchi and J. C. Booth, *Biomicrofluidics*, 2011, **5**, 044107.
45 S. Li, X. Ding, F. Guo, Y. Chen, M. I. Lapsley, S.-C. S. Lin, L. Wang, J. P. McCoy, C. E. Cameron and T. J. Huang, *Anal. Chem.*, 2013, **85**, 5468–5474.
46 B. Jung, K. Fisher, K. D. Ness, K. A. Rose and R. P. Mariella, *Anal. Chem.*, 2008, **80**, 8447–8452.
47 J. Brody and P. Yager, *Proc. Solid-State Sens. Actuator Workshop*, 1996, 105–108.
48 B. H. Weigl and P. Yager, *Science*, 1999, **283**, 346–347.

49 P. Krulevitch, W. Benett, J. Hamilton, M. Maghribi and K. Rose, *Biomed. Microdevices*, 2002, **4**, 301–308.
50 P. Augustsson, R. Barnkob, S. T. Wereley, H. Bruus and T. Laurell, *Lab Chip*, 2011, **11**, 4152.
51 M. A. Epstein, B. G. Achong, Y. M. Barr, B. Zajac, G. Henle and W. Henle, *J. Natl. Cancer Inst.*, 1966, **37**, 547–559.
52 S. Sriurairatna, N. Bhamarapravati and O. Phalavadhtana, *Infect. Immun.*, 1973, **8**, 1017–1028.
53 A. H. J. Yang and H. T. Soh, *Anal. Chem.*, 2012, **84**, 10756–10762.
54 P. Augustsson, C. Magnusson, M. Nordin, H. Lilja and T. Laurell, *Anal. Chem.*, 2012, **84**, 7954–7962.
55 F. Petersson, L. Aberg, A.-M. Swärd-Nilsson and T. Laurell, *Anal. Chem.*, 2007, **79**, 5117–5123.
56 P. B. Muller, R. Barnkob, M. J. H. Jensen and H. Bruus, *Lab Chip*, 2012, **12**, 4617.